Structural, optical and magnetic properties of Gd/TiO$_2$-reduced graphene oxide nanocomposites

N. Nithyaa[1] · M. Muralidharan[2] · N. Victor Jaya[1]

Abstract

The focus of the present work is to study the effect of reduced graphene oxide (rGO) on morphology, crystal structure and magnetic properties of Gadolinium (Gd)-doped TiO$_2$ nanoparticles. Gd/TiO$_2$-rGO nanocomposites are synthesised in two steps: sol–gel and hydrothermal method. The prepared composites are studied with XRD, Raman, HRTEM, PL, EPR and VSM for further analysis. XRD and HRTEM studies elucidate the crystallinity of the nanocomposite decreases with increase in Gd concentration. Electron micrographs of the samples reveal that both pure TiO$_2$ and Gd/TiO$_2$ nanoparticles are evenly decorated on the graphene sheets. Raman and PL spectroscopic techniques confirm the presence of oxygen vacancies (Vo) and surface defects. Enhanced optical absorption shows the interaction between Ti–Gd with rGO composites. Decrease in bandgap values may be understood by quantum confinement effect. The presence of singly ionised Vo is confirmed from EPR spectra which is responsible for weak ferromagnetic behaviour at room temperature. Moreover, magnetic studies show the concurrency of ferromagnetic and antiferromagnetic interaction that originates from different defects present in the Gd/TiO$_2$-rGO nanocomposites.

1 Introduction

Carbon materials are of special attraction because of its bonding nature, formation of large stable frameworks, different hybridisations and dimensions, etc. [1]. Graphite, a carbon allotrope with three dimensions consists of stacked graphene layers, whereas graphene is two-dimensional with a single layer of carbon atoms arranged in a honeycomb lattice order [2, 3]. Graphene, the thinnest and strongest material in the universe, also has exceptional properties such as high specific surface area (2630 m^2 g^{-1})^2 [4], superior carrier mobility at room temperature (10,000 cm^2 V^{-1} s^{-1}) [5], high thermal conductivity (3000–5000 Wm^{-1} K^{-1}) [6], enhanced optical transparency [7]. In addition, intrinsic room temperature ferromagnetism occurs with various defects in graphene structures, such as edge defects, vacancy, topological changes, hydrogen chemisorptions, frustration [8]. Magnetic transitions among dia-, para-, antiferro- and superparamagnetism are also possible [9].

Recently, there are several reports on room temperature magnetic properties of wide bandgap metal oxides [10, 11]. Nanoparticulate of metal oxides exhibits room temperature ferromagnetism unlike their bulk forms. Spin manipulation and increased carrier mobility of graphene make it possible to use both spin and charge of a material, a favourable property applicable for spintronic materials [12]. But to harness its interesting uncommon properties, integrating graphene with other materials (metals, semiconductor, polymers and other carbon materials) is necessary to form efficient composite materials [13]. These nanocomposite structures have inherited merits such as large surface area, large surface-to-volume ratio, porous structure, superparamagnetism, strong adsorption ability and chemical stability. Lee et al. [14] report dangling bonds between interlayer and inter edges are responsible for ferromagnetism of stacked graphitic fragments. Intrinsic magnetic nature of graphene nanoribbons with coexistence of antiferromagnetic regions and ferromagnetic clusters are reported by Rao et al. [15]. Lattice defects and RKKY interaction of local moments caused by

✉ N. Nithyaa
    kishnithi@gmail.Com

1   Department of Physics, Anna University, Chennai, Tamil Nadu 600025, India

2   Department of Material Science, University of Madras, Chennai, Tamil Nadu 600025, India

electron–electron interaction in graphene planes result in ferromagnetism which confirms graphene to be a semimetal [16]. Pisani et al. [17] reported a defective graphene sheet with point defects in an array will generate RTFM, where defect concentration is responsible for magnetic coupling and energy gap. Therefore, graphene is an ideal base for multifunctional materials and appears to improve the magnetic properties.

Hence, by combining these metal oxide systems in reduced particle size and prominent qualities of graphene we can obtain tunable ferromagnetic compounds which may find application in magnetic memory devices, spintronics, magnetoresistance, magneto-biomedical and so on. Theoretical and magnetic measurements confirm ferromagnetic properties of graphene/Co composite arising from partial oxidation of metal oxides [18]. Graphene oxide–Fe_3O_4 exhibits superparamagnetic behaviour with high magnetisation values for use in controlled and targeted drug delivery [19]. Hydrothermally prepared graphene/SnO_2 flower structures show high lithium ion battery performance with superior cyclic performance and excellent reversible capacity [20]. Graphene scaffolds with Pt/Au metal catalysts are reported as excellent hydrogen storage pathways [21].

Among these, TiO_2 is on outstanding binary oxide ($Eg = 3.2$ eV) semiconductor with unique properties such as non-toxic, cost effective, eco-friendly and extensive spintronic applications. Another interesting feature is pristine TiO_2 demonstrates ferromagnetism at 300 K due to intrinsic point defects and Ti vacancies [22]. TiO_2 nanostructures exhibit ferromagnetism by the introduction of transition or rare-earth metal dopants, topological defects and oxygen vacancies [23–25]. Besides various rare-earth ions, gadolinium is of great interest with its large magnetic moment, high number of unpaired electrons, atomic and paramagnetic properties [26]. Effect of Gd ion on various metal oxides has been investigated [27, 28]. Doping of Gd ions in SnO_2 exhibits ferromagnetic signature because of exchange interactions between dopants and host matrix ions [29]. Gd-doped ZnO thin films are extensively studied where oxygen deficiencies related to Gd defect complexes result in long-range ferromagnetism suitable for spin injection in DMS materials [30, 31]. Localised unpaired spins due to various edges, site defects, point defect like vacancies induce ferromagnetism in graphene-TiO_2 nanocomposite [32].

However, there are numerous reports on Gd-doped TiO_2 for photocatalytic and DSSC applications; conversely, the present work focuses on the magnetic property of the Gd-doped TiO_2 with graphene composites which are scarcely reported. Hence, the motivation of this work is to study the structural, optical and magnetic behaviour of Gd-doped TiO_2 graphene composites synthesised by hydrothermal method. Various characterisation techniques are carried out and the results are presented herein.

2 Experimental

2.1 Materials

The chemicals used are of analytical grade (Alfa Aesar, 99.9%): Graphite Powder, Potassium Permanganate ($KMnO_4$), Conc.Orthophosphoric Acid (H_3PO_4), Conc. Sulphuric Acid (H_2SO_4), Hydrogen Peroxide (H_2O_2), ethanol (C_2H_5OH) and deionised water.

2.2 Preparation of graphite oxide

Graphite oxide is prepared using graphite powder with modification in improved Hummers method at room temperature [33]. To start with, 1.6 g of graphite flakes is added to a mixture of 160 ml of Conc.sulphuric acid (98%) and 40 ml of Conc.orthophosphoric acid (85%) in a 4:1 ratio under vigorous stirring. At regular interval, 9 g of potassium permanganate is added in small quantities to the above solution. For complete oxidation of the precursor, the prepared solution is left under constant stirring for 72 h. The resulting dark brown coloured solution changes to yellow colour with addition of appropriate amounts of hydrogen peroxide reacting exothermically indicating complete oxidation of the solution. The resultant is washed several times with warm water and 1 M hydrochloric acid to remove the residual sulphate ions and neutralise the pH of the solution. The resulting dark brown colloidal precipitate is dried at 80 °C to obtain black coloured sheets. These sheets are grounded using a mortar to obtain powders of graphite oxide (GO).

2.3 Preparation of Gd/TiO_2-rGO composites

Pure TiO_2 and gadolinium ion-doped TiO_2 nanoparticles are synthesised by sol–gel method as reported in our previous work [34]. Gd/TiO_2-rGO composites are prepared by hydrothermal method. For exfoliation, 30 mg of prepared graphite oxide (GO) powder dispersed in water and ethanol (2:1 ratio) is under ultrasonication for 2 h. To the above, 300 mg of TiO_2 or Gd/TiO_2 with different atomic ratios of Gd (1%, 3% and 5%) is added and stirred for 2 h to obtain a homogeneous solution. The solution is then transferred into an autoclave and maintained at 120 °C for 3 h which aids in the reduction of graphene oxide (rGO) and TiO_2 nanoparticles to deposit on the graphene sheets simultaneously [35]. The aftereffect solution is collected and washed with deionised water for several times and dried at 80 °C for 12 h. Finally, the composites of TiO_2 and Gd/TiO_2 (1%, 3% and 5%) obtained by above procedure are named GOT, GGT1, GGT3 and GGT5, respectively, for further characterisations.

In this communication, reduced graphene oxide (rGO) is also referred as graphene.

2.4 Material characterisation

X-ray diffraction analysis is done with BrukerD8 advanced powder X-ray diffractometer using CuKα ($\lambda = 0.15406$ nm) in the 2θ range 5°–80°. Raman spectra are recorded with Horiba Jobin Yvon LabRAM HR using Ar-Ion gas laser with the excitation source of 514 nm at room temperature. Surface texture is imaged using FEI Quanta FEG 200-field emission scanning electron microscope (FESEM) aided with EDAX analysis. HRTEM analysis is done using JEOL JEM-2010 transmission electron microscope. Specific surface area and pore size analysis is studied using micromeritics Model ASAP 2020 with liquid nitrogen (77 K) as absorbate. UV–Vis diffuse reflectance spectra (UV-DRS) are measured using a Jasco V-700 spectrometer. The photoluminescence (PL) spectra are recorded with spectrofluorometer under an excitation of wavelength 315 nm. Electron paramagnetic resonance spectra and M–H hysteresis curves of composites are recorded at room temperature using Bruker TMX spectrometer and Lakeshore VSM7410 instrument, respectively.

3 Results and discussion

3.1 XRD studies

Crystalline nature and phase identification of pure TiO_2 and Gd/TiO_2-rGO composites are studied and presented in Fig. 1a and b. XRD of graphite oxide (GO) is shown in Fig. 1a. The diffraction pattern of the as-prepared graphite oxide exhibits its typical characteristic peak at $2\theta = 10.5°$ corresponding to (001) reflection with an interlayer spacing, $d = 0.84$ nm calculated from Bragg's equation [36]. This increased 'd' spacing from that of pure graphite is related to various oxygen functional groups like hydroxyl, epoxide and carboxyl groups present in its lattice [37]. From Fig. 1b, the appearance of diffraction peak at 25.68°, 38.4°, 48.79°, 54.77°, 55.21°, 63.13°, 69.06°, 70.44° and 75.28° is indexed to the reflection planes of (101), (004), (200), (105), (211), (204), (116), (220) and (215) matching well with anatase phase of TiO_2 (JCPDS-00-075-1537). This reveals the unchanged crystal structure of TiO_2 after their assembly on rGO sheets. After hydrothermal reduction and formation of reduced graphene oxide (rGO) nanosheets, the characteristic diffraction peak of rGO is not visible in the diffraction pattern of nanocomposites, due to the intercalation of pure and Gd/TiO_2 nanoparticles into stacked graphene layers or the characteristic
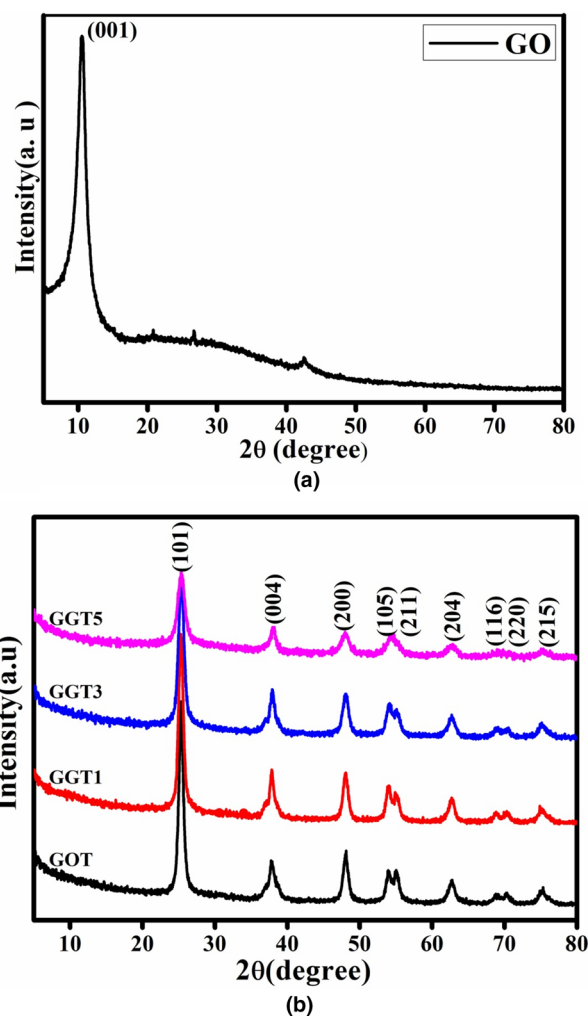

Fig. 1 **a** PXRD pattern of the as-prepared graphite oxide. **b** PXRD pattern of pristine TiO_2 and Gd/TiO_2-rGO composites

diffraction peak of TiO_2 at 25.68° may overlap [38]. The average crystallite sizes of all samples are estimated from Scherrer equation and are listed in Table 1. The diffraction peak broadening with increase in dopant concentration (Fig. S1) indicates the decreasing trend of crystallite size. Decrement in crystallinity is evitable from the blunt and less intense diffraction peaks of GGT3 and GGT5 samples. The Williamson–Hall plots are made to determine the crystallite size and strain from the intercept and slope of linear fit plot of $\beta Cos\theta$ and $4Sin\theta$ (as shown in Fig. S2). The calculated lattice parameter values, crystallite size and lattice strain samples are summarised in Table 1. From the table, pure TiO_2 graphene composites show increased strain values than Gd/TiO_2 graphene composites due to imperfections in the crystalline lattice. Hence, powder XRD studies confirm the formation of pure and Gd/TiO_2 graphene composites.

Table 1 Crystal structural parameters of pure TiO$_2$ and Gd/TiO$_2$-rGO composites

Sample	Lattice parameters (Å)		c/a ratio	Unit cell volume (A^3)	Crystallite size (nm)		Lattice strain (10^{-3})
	$a=b$	c			Scherrer	W–H	
TiO$_2$	3.7745	9.3985	2.48998	133.89	7	15	8.2
GOT	3.7872	9.4555	2.4967	135.62	8	12	3.89
GGT1	3.7840	9.4974	2.50988	135.99	12	15	1.65
GGT3	3.7834	9.4796	2.50557	135.69	10	12	0.631
GGT5	3.7831	9.4871	2.50775	135.78	9	10	0.426
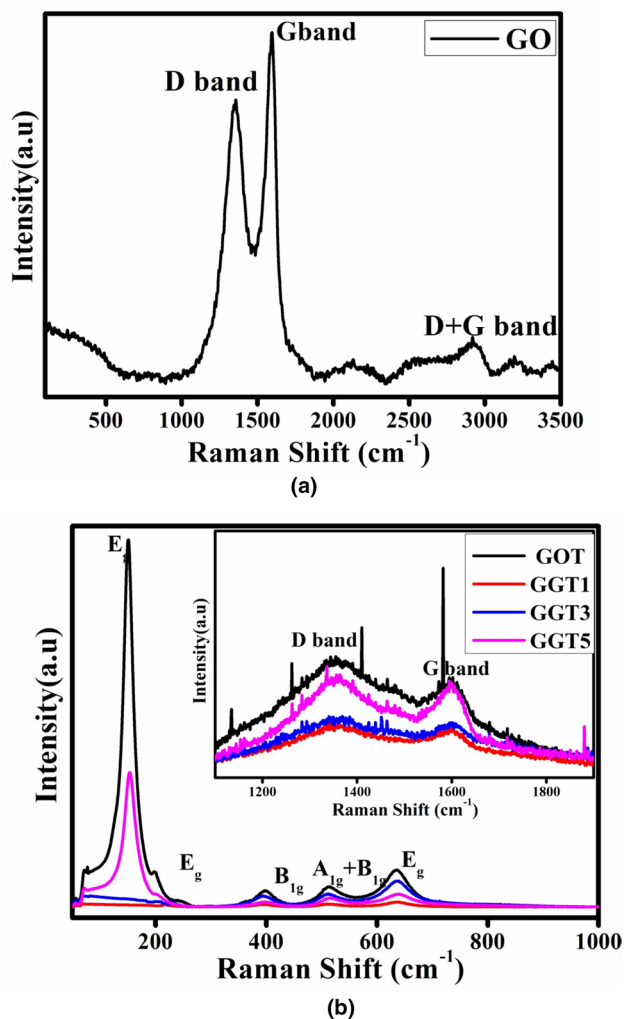
Fig. 2 **a** Raman spectra of the as-prepared graphite oxide. **b** Raman spectra of pure TiO$_2$ and Gd/TiO$_2$-rGO composites. Inset shows magnification of curves in 1000–2000 cm^{-1} range

3.2 Raman studies

Raman spectroscopy is a sensitive tool to analyse the crystalline quality of carbon-based materials. Figure 2a displays the Raman spectra of the pristine graphite oxide at 514 nm, which exhibit two characteristic peaks around 1352 and 1595 cm^{-1}, corresponding to D band originating from the structural disorders and other defects capable of breaking the symmetry and selection rule, and G band originating from the C–C bond stretching of sp^2 carbon pairs, respectively [39]. It also shows the combination band (D + G) at 2924 cm^{-1} resulting from the defect density in GO [40]. In addition, there are less intense peaks at 2555 and 3200 cm^{-1} corresponding to D + D' and 2D' bands due to double resonance confirming the multilayer structure [41]. Figure 2b shows the Raman spectra of pure and Gd/TiO$_2$-rGO composites with its inset showing high wavenumber region. The entire prepared graphene composites exhibit both the allowed active Raman modes of anatase phase of TiO$_2$ and the characteristics peak of GO. Both G and D bands of composites are blue shifted corresponding to prepared graphite oxide (GO) (Fig. S3). The G band in Raman spectra of GO appears at 1595 cm^{-1}, whereas for GOT composite it is moved to 1579 cm^{-1} (approximately close to pristine graphite) which confirms the reduction of graphite oxide [42]. From the figures, the intensity of D band is found comparatively less for GO than the rGO composites showing that more disordered carbon structures are produced after the exfoliation and hydrothermal process [43]. The extent of disorder is given by the intensity ratio of D band to G band (I$_D$/I$_G$). The intensity ratio is found to be higher for the GOT sample (1.2) and GGT samples (1.1) than GO (0.98) indicating increased lattice disorders in rGO composites than GO which complements the XRD result. The non-appearance of 2D peak in the spectrum of composites indicates maximum distortion of sp^2 network bonds [44]. These structural details confirm the occurrence of oxygen vacancies and defects in both pure TiO$_2$ and Gd/TiO$_2$ graphene nanocomposites.

3.3 Morphological studies

3.3.1 FESEM analysis

Direct evidence of the formation of nanocomposites is shown by SEM micrographs. Figure 3 shows the images of Gd-doped TiO$_2$ and its graphene composites. The pure
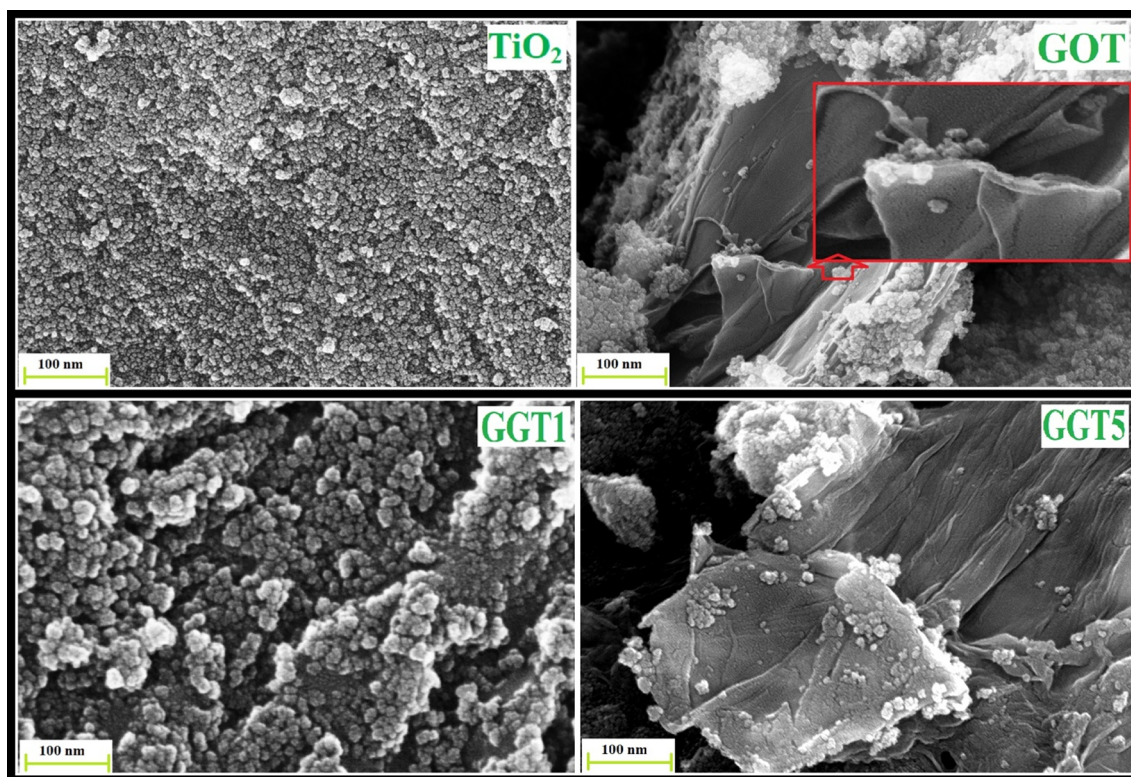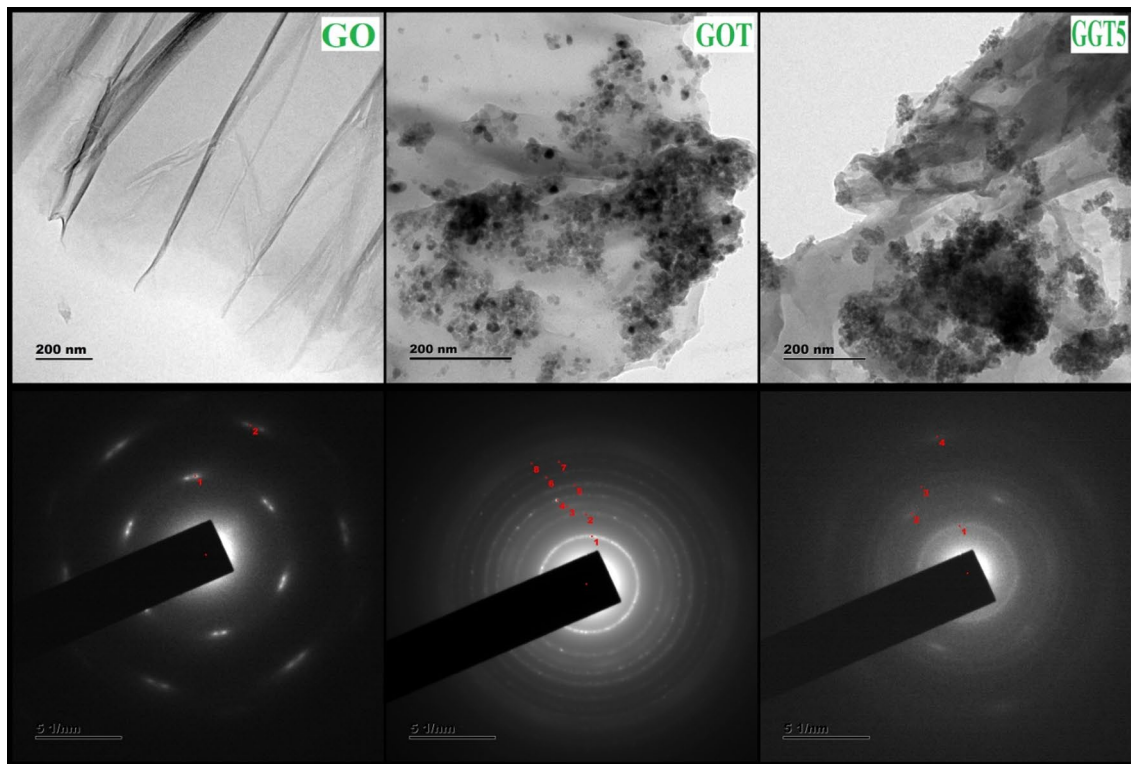
Fig. 3 FESEM images of pure TiO$_2$ and Gd/TiO$_2$-rGO nanocomposites

TiO$_2$ nanoparticles show irregular spherical shaped particles with aggregation and an average size around 20 nm. Graphene sheets generally aggregate forming stacked multilayers. The inset image depicts a uniform and dense distribution of TiO$_2$ nanoparticles on both sides of the graphene nanosheets, which is in agreement with XRD results. GGT1 and GGT5 images show irregular zigzag edges with Gd/TiO$_2$ nanoparticles aggregated or uniformly distributed on the sheets [39, 45]. This self-assembling of TiO$_2$ and Gd/TiO$_2$ nanoparticles seems to occur during the hydrothermal preparation method. From the morphological studies, it is clear that both TiO$_2$ and Gd/TiO$_2$ are well dispersed on graphene sheets which act as a substrate or supporting material. These reduced graphene oxide sheets with some functional groups retained on it increase the binding affinity of TiO$_2$ nanoparticles. The well-adhered nanoparticles increase the localisation of electronic pairs, edge states and covalent bonding of itinerant atoms. TiO$_2$ and Gd/TiO$_2$ nanoparticles are also intercalated into stacked graphene sheets which increase the edge state spins of graphene thereby enhancing the magnetic behaviour of the composite [46]. The energy dispersive X-ray (EDAX) spectra are further used to reveal the chemical content of the samples (Fig. S4) wherein the peak of C is related to reduced graphene oxide. It also shows the contents of O, Ti and Gd elements present in the synthesised nanocomposite.

3.3.2 HRTEM analysis

For further confirmation of decoration of TiO$_2$ nanoparticles on the graphene sheets and to study the surface texture of the samples, transmission electron microscopy (TEM) analysis is carried out. Figure 4a shows the high-resolution TEM images of pure and Gd/TiO$_2$-rGO nanocomposites along with its corresponding SAED pattern. The TEM images also demonstrate that TiO$_2$ and Gd/TiO$_2$ nanoparticles are deposited on graphene sheets. The as-synthesised GO sheets exhibit flake-like structure with wrinkles and folding towards the surface and edges. The sheet structures of graphene composites remain unaffected by the hydrothermal synthesis procedure. The TiO$_2$ and Gd/TiO$_2$ nanoparticles are well dispersed on thin layered and transparent rGO sheets which are likely to interact because of the distribution of functional groups on it [45]. The selected area electron diffraction (SAED) pattern of GO shows discontinuous circle and GOT sample shows bright diffraction rings which can be indexed to crystal planes of tetragonal structure of anatase phase of TiO$_2$. Besides GGT5 exhibit less intense rings indicating the decrease in crystallinity which is in compliance
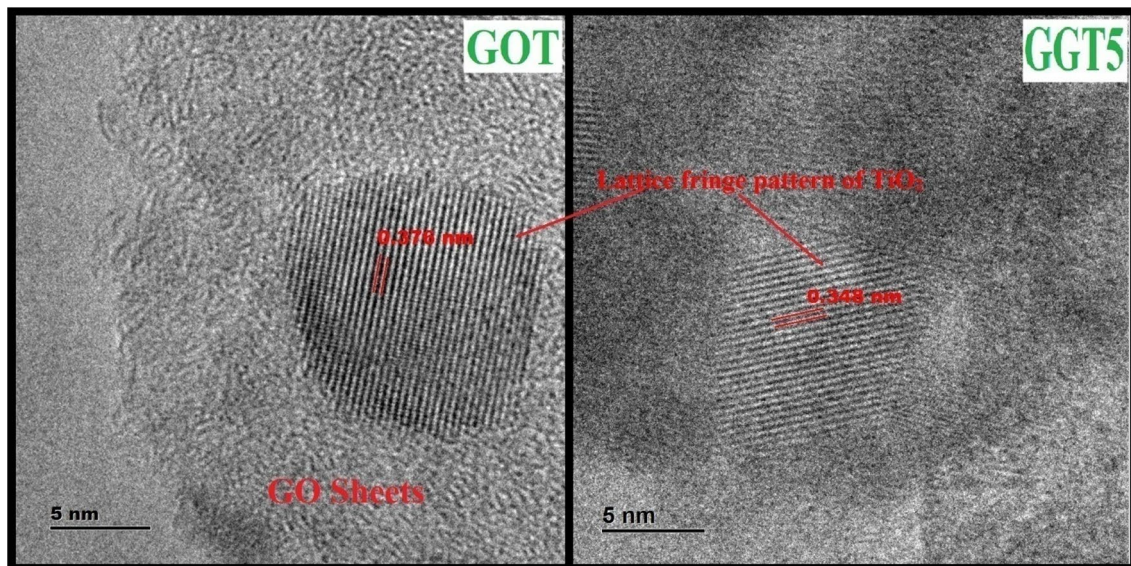
Fig. 4 **a** HRTEM images of graphite oxide, pure TiO$_2$ and 5% Gd/TiO$_2$-rGO composites and its corresponding SAED pattern. **b** Low-magnification HRTEM images of pure TiO$_2$ and 5% Gd/TiO$_2$-rGO nanocomposites

with the results of powder XRD analysis. From Fig. 4b, in addition to the fringes of TiO$_2$ particles, the fringes of rGO are also visible confirming the binding of TiO$_2$ to rGO. The lattice fringes shown herein with d-spacing can be marked to the plane (101) of TiO$_2$ in the composite. An energy dispersive X-ray spectrum (EDS) further affirms the purity of the sample. Figure S5 reports the presence of C, Ti, Gd and O elements without any impurities. The occurrence of copper
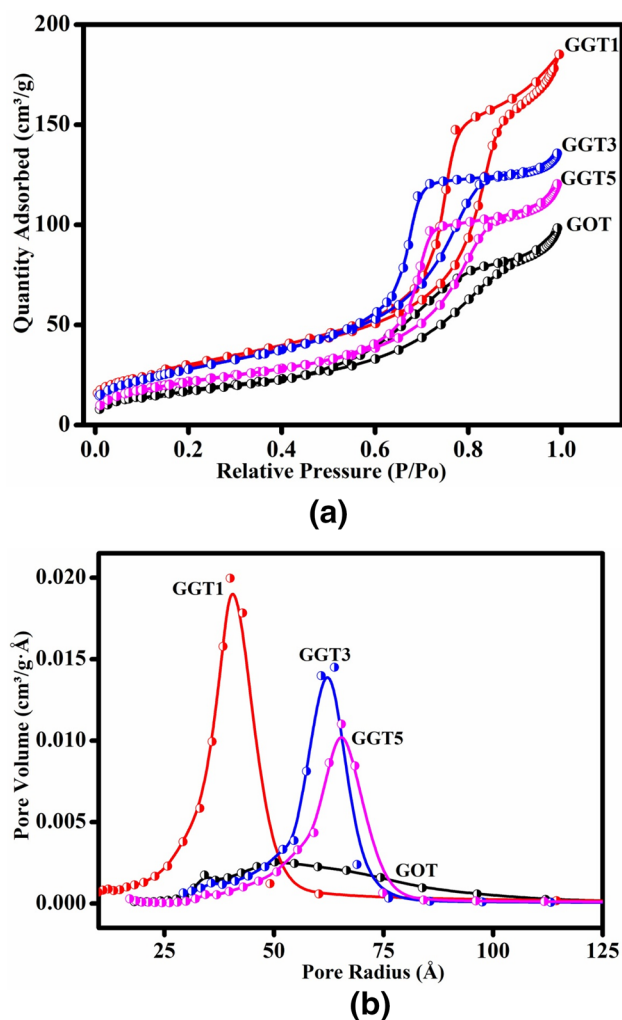
(a)

(b)

Fig. 5 a N_2 Adsorption–desorption isotherms of pure TiO_2 and Gd/TiO_2-rGO composites. **b** Distribution of pore size for pure TiO_2 and Gd/TiO_2-rGO composites

ion arises from the copper grid which is used for HRTEM analysis.

3.3.3 Textural analysis

To determine the surface area and porosity of prepared graphene composites, nitrogen adsorption–desorption isotherm measurements are carried out and presented in Fig. 5a. The adsorption hysteresis loop of pure TiO_2 and Gd/TiO_2-rGO composites are similar and represent the type IV isotherm which evidently proves the mesoporous structure of the prepared materials. Surface area of the as-prepared graphite oxide (GO) is found to be 3.3315 m^2 g^{-1} prior to exfoliation, whereas the synthesised nanocomposites exhibit a higher surface area shown in Table 2 (less than the theoretical reported value) after proper exfoliation and hydrothermal reduction of the prepared GO. A low surface area value for GOT composite is attributed to the improper exfoliation and stacked morphology of the graphene sheets [47, 48]. This effect leads to the restoration of more hydroxyl and oxygen functional groups in the graphene lattice which aids in maximising the defects or oxygen vacancies in the lattice. Barrett–Joyner–Halenda (BJH) data are used to plot pore size distribution, as shown in Fig. 5b. Textural data such as surface area, pore volume (Vp), pore radius and particle size calculated from BET surface area are compiled in Table 2. Gd/TiO_2 graphene composites exhibits increased surface area than pure TiO_2 graphene composites. This increase in surface area is a result of uniform anchoring of Gd/TiO_2 nanoparticles on the graphene sheets surface preventing aggregation of graphene layers [36]. However, the values of surface area are found increasing for GGT composites. It is also seen that the pore volume and pore radius gradually decrease with increase in Gd doping.
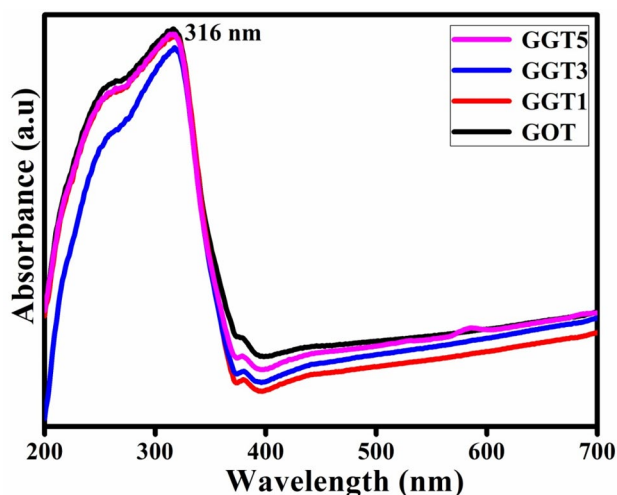
Table 2 Textural parameters of pure TiO_2 and Gd/TiO_2-rGO nanocomposites

Sample	Surface area (m^2 g^{-1})	Pore volume Vp (cm^3 g^{-1})	Pore radius r (Å)	Particle size (nm)
TiO_2	88.411	0.211694	25.727	18
GOT	63.6344	0.152040	30.152	24
GGT1	102.4171	0.286314	46.400	14
GGT3	101.0609	0.209885	31.874	15
GGT5	79.2488	0.186157	29.414	19

Fig. 6 Absorption spectra of pure TiO_2 and Gd/TiO_2-rGO composites

3.4 Diffuse reflectance UV–Vis spectra analysis

Visible light absorption is being studied using diffuse reflectance UV–Vis spectroscopy (DRS-UV). Figure 6 shows the optical absorption spectra of pure TiO_2 and Gd/TiO_2-rGO composites. Irrespective of Gd doping and graphene incorporation, the absorption maxima of pure GOT and GGT samples are almost the same and at around 316 nm, which is still in the ultraviolet region. The energy gap between the conduction and valence bands of formed nanocomposites are determined from Kubelka–Munk plot (shown in Fig. S6) by extrapolation and intersection of the linear portion of $(\alpha h\nu)^2$ to the energy axis $h\nu$. The bandgap values of GOT, GGT1, GGT3 and GGT5 are 3.35, 3.44, 3.41 and 3.45, respectively. Generally, rare-earth ion-doped and graphene-incorporated TiO_2 show enhanced optical properties than pure TiO_2. Conversely, here their contribution is trivial owing to their small grain size which results in quantum confinement effect. The energy bandgap of GGT samples is higher than the GOT sample and this can be attributed to reduction in their crystallite size and the dopant ions may introduce new electronic amidst the energy band of the composites [49]. Li. et al. [50] report, when graphene content in the composite increases, bandgap narrowing occurs, but here stoichiometry composition of graphene is less when compared to pure TiO_2 and Gd/TiO_2 which may result in increase in bandgap.

3.5 Photoluminescence studies

Photoluminescence spectra report the presence of intrinsic defects in pure TiO_2 and Gd ion-doped TiO_2 graphene nanocomposites as shown in Fig. 7. The emission spectra of pure TiO_2 an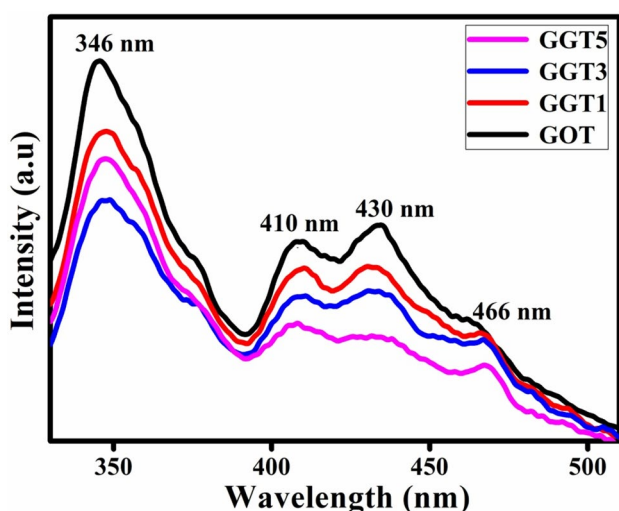d Gd/TiO_2-rGO composites show similar visible band emission in the range of 300–500 nm. As shown in the spectra, the intensity of GOT is highest and GGT5 shows the lowest intensity among all the samples. Generally, the loading of TiO_2 or Gd/TiO_2 on the graphene sheets facilitates suppression of recombination of photogenerated carriers thereby decreasing the emission intensity [51]. This decrease in emission intensity may also result from gadolinium doping slowing down the electron and hole recombination [34]. The emission peak seen at 346 nm in all the samples attributes to the characteristic band edge emission. Though for GGT5 the intensity of visible emission peaks is less than GGT3, the band edge emission intensity is higher because the generated charge carriers are localised at different defect sites on the surface of Gd/TiO_2-rGO nanocomposites [52]. The violet emission at 410 nm may be due to the shallow surface defects, and the two peaks around 430 nm and 466 nm in the visible region generally observed for TiO_2 nanoparticles are assigned to defects or defect levels connected with oxygen vacancies or grain boundaries or dangling bonds in rGO sheets [53]. The emission peak at 466 nm in graphene composites might also be related to the π–π^* transitions of GO [54]. From Fig. 7, it is seen that while increasing dopant concentration, the absorption maxima shifted towards higher wavelength indicating the strong optical absorption behaviour.

3.6 Electron paramagnetic studies

EPR is an important tool used to determine the interaction between the unpaired electrons and the magnetic field. It also examines the oxidation state of metal ions [55]. Room temperature EPR spectra of pure TiO_2 and Gd/TiO_2-rGO nanocomposites are imaged and shown in Fig. 8. The high-intensity peaks are of Gd-doped TiO_2 graphene composites, whereas pure TiO_2 graphene samples show low-intensity
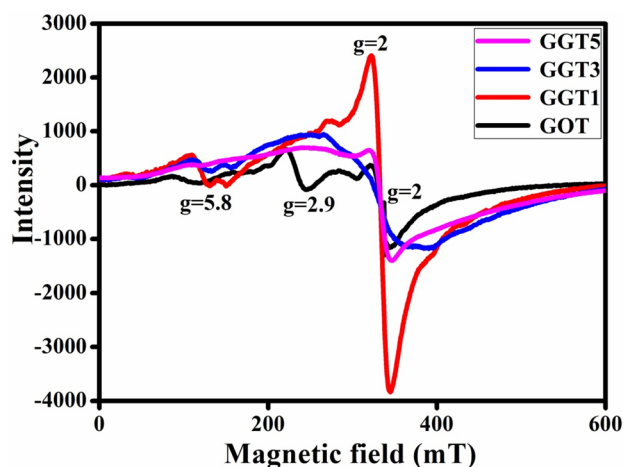
Fig. 7 Photoluminescence spectra of pure TiO_2 and Gd/TiO_2-rGO composites

Fig. 8 EPR spectra of pure TiO_2 and Gd/TiO_2-rGO nanocomposites

EPR signals. This hyperfine magnetic interaction reveals the paramagnetic centres are not identical and there exist various levels of morphological heterogeneity and surface imperfections causing defects in the prepared samples [56]. EPR parameter 'g' calculation allows us to determine the types of defects present in the prepared composites. The 'g' factor is calculated using the relation

$$g = \frac{h\nu}{BH},\tag{1}$$

where H is the magnetic field (mT), ν is the resonance frequency (Hz), h and B are the Planck's constant and Bohr magneton, respectively [57]. The EPR spectra of GOT composite exhibit a hyperfine structure with a broad intense peak ($g = 2.009$) superimposed on a prominent sharp peak ($g = 1.99$) indicating the presence of both graphene and surface Ti^{3+} ions in the samples or surface-related oxygen vacancies [58]. This implies that both the carbon inherited spin species and rare-earth metal impurities are responsible for free electron 'g' value which generates oxygen vacancies and interfacial defects in the lattice [59]. In addition to the strong EPR signal, GOT composite also shows few less intense EPR signal ($g = 2.1, 2.7$ and 3.06) due to surface imperfections and related defects. The magnetic anisotropy components and various types of magnetic centres cause the difference in the 'g' values of the composites [60]. The GGT samples also follow the same pattern of EPR signals as GOT composite but with increased intensity for GGT1 and less intense peaks for GGT3 and GGT5 along with gadolinium characteristic peaks ($g = 2$ and 5.9) indicating the presence of Gd^{3+} ions in the composites [61, 62]. These evidence the presence of singly ionised oxygen vacancies and π electrons in the graphene composites which aids in the magnetic property of the prepared composites.

3.7 Magnetisation studies

Though bulk graphene is non-magnetic in nature, its derivatives show room temperature ferromagnetism, its origin being a topic of academic interest. This type of inherited magnetism arises from edge states [63], defects such as single atom defects, vacancies, stacking faults of graphene sheets [64], and localised unpaired electron spins arising from surface and dangling bonds [65]. In its focus, when semiconducting oxides like TiO_2 are deposited on graphene scaffold during the synthesis of nanocomposites, it increases the magnetic moment of the composite by charge transfer interaction, thereby increasing the chances of room temperature ferromagnetism [66]. The magnetisation hysteresis loops of pure TiO_2 and Gd/TiO_2-rGO composites at room temperature are presented in Fig. 9. The field-dependent magnetisation (M–H) curve of GOT composite shows unsaturated weak ferromagnetic behaviour,
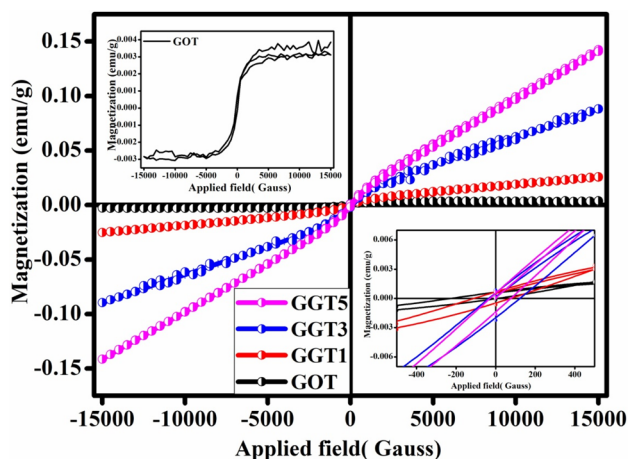

Fig. 9 M–H curves of pure TiO_2 and Gd/TiO_2-rGO nanocomposites

Table 3 Magnetisation values of pure TiO_2 and Gd/TiO_2-rGO Nanocomposites

Sample	Coercivity (Hc) Gauss	Saturation Magnetisation ($Ms \times 10^{-3}$ emu g^{-1})	Remanent magnetisation ($Mr \times 10^{-3}$ emu g^{-1})
TiO_2	124.89	0.162	0.022
GOT	134.12	0.106	0.013
GGT1	105.52	0.486	0.014
GGT3	88.432	1.777	0.021
GGT5	59.427	3.833	0.030

whereas GGT composites exhibit ferromagnetic interaction at lower magnetic field and unsaturated ferromagnetic interaction at higher magnetic field. However, theoretical and experimental studies figure out the coexistence of ferromagnetic along with antiferromagnetic behaviour in graphene-related materials depending on various defects and disorder, chemical doping, vacancies, edge states and the attachment of functional groups [9]. At nanoscales, ferromagnetism is an intrinsic property of metal oxides because of an increase in surface to volume ratio of the nanomaterials [67]. Oprea et al. report increased magnetic moment and hysteresis in Gd-doped ZnO due to partially filled 5d and 4f orbitals presented by Gd ions [68]. Thiyagarajan et al. discuss the concurrence of ferro- and antiferromagnetic behaviour of rGO- WO_3 nanorods owing to oxygen vacancies and surface defects [69]. Xiang et al. [70] prepared highly crystalline Co-doped ZnO/reduced graphene oxide core–shell hybrid nanoparticles showing canted antiferromagnetic behaviour for its utilisation in dilute magnetic semiconductor quantum dots (DMSQD). Impact of Gd and graphene incorporation in magnesium ferrites studied by Atiea et al. shows enhancement in saturation magnetisation owing to extrinsic (morphology,

crystallite size) and intrinsic (changes in coordination of atoms, surface disorders) parameters [71].

The magnetic parameters, namely coercivity, saturation and remanent magnetisation, are studied from hysteresis loops and summarised in Table 3. The coercivity of GOT composite increases with inclusion of rGO which is attributed to surface spin effects resulting from exchange and dipolar interactions between the particles [72]. Thus, the pure GOT samples intrinsic magnetic property is suppressed and it exhibits weak ferromagnetism. However, inclusion of Gd in TiO_2 lattice causes a decrease in coercivity values of GGT samples likely due to paramagnetic contribution of Gd ions. This is also evident from PL and EPR analyses whose intensity decreases compared to GOT sample. It is also considerable that decrease in oxygen vacancy may disturb the weak ferromagnetic order exhibited by GOT sample. However, their magnetisation saturation value increases with increase in dopant concentration mainly due to doped Gd ions disturbing the local symmetry causing internal stress and crystal strains there by increasing the magnetic domain wall. The M–H loop of GGT nanocomposites shows ferromagnetism at low fields caused by edge effects of graphene sheets, oxygen containing functional groups and antiferromagnetism at high fields is resulting from graphene sheet nature and Gd–Gd interaction between Gd ions in TiO_2 lattice [59]. As the dopant concentration increases, the antiferromagnetic behaviour turns into paramagnetic nature due to Gd-V_o-Gd interaction as reported earlier [34].

In our earlier work, weak ferromagnetism in TiO_2 is reported to defects like Ti vacancies, oxygen vacancies, surface and stoichiometry [34]. This weak ferromagnetism with saturation values being very low is deposited on graphene sheets to enhance its magnetic parameters. As a result of charge transfer complexes and magnetic coupling, coercivity (Hc) increases for pure TiO_2 graphene composites but saturation magnetisation (Ms) decreases, whereas Gd-doped TiO_2 graphene composites show increased Ms value and decreased coercivity. This decrease in Ms value may also result from composite stoichiometry where graphene and TiO_2 or Gd/TiO_2 is in the ratio of 1:10. Thus, the spin polarisation of graphene sheet edges and the spin alignments of nanodomains of nanoparticles together tune the ferro- and antiferromagnetic property of Gd/TiO_2 graphene nanocomposites [73].

4 Conclusion

To summarise, pure TiO_2 and Gd/TiO_2 graphene nanocomposites synthesised by hydrothermal method are studied for its structural, optical and magnetic properties. XRD reveals the tetragonal anatase crystalline structure of the composites. The increased intensity of D band in Raman spectra confirms the presence of local structural distortion in the composites. Morphological studies show the Gd/TiO_2 spherical particles are distributed and decorated on surface of graphene sheets. The Gd/TiO_2-rGO nanocomposite demonstrates enhanced optical behaviour with optical energy gap delivering the decrease in crystallinity and quantum confinement effect in prepared composites. Multicolour emission from PL spectra and the 'g' parameter of nanocomposites confirm both graphene and Gd ions are responsible for the defect existence in the composites. The surface spins and surface defects of the graphene nanocomposites cause ferromagnetic and antiferromagnetic interaction. Hence, structure, size and shape influence the optical and magnetic properties of nanocomposites which may be a hopeful material for DMS-based applications.

References

1. Y. Yang, C. Han, B. Jiang, J. Iocozzia, C. He, D. Shi, T. Jiang, Z. Lin, Mater. Sci. Eng. R **102**, 1 (2016)
2. P.R. Wallace, Phys. Rev. **71**, 622 (1947)
3. J. Tsuneya Ando, Phys. Soc. Jpn. **74**, 777 (2005)
4. M.D. Stoller, S. Park, Y. Zhu, J. An, R.S. Ruof, Nano Lett. **8**, 3498 (2008)
5. K.S. Novoselov, A.K. Geim, S.V. Morozov, D. Jiang, Y. Zhang, S.V. Dubonos, I.V. Grigorieva, A.A. Firsov, Science **306**, 666 (2004)
6. A.A. Balandin, S. Ghosh, W. Bao, I. Calizo, D. Teweldebrhan, F. Miao, C.N. Lau, Nano Lett. **8**, 902 (2008)
7. R.R. Nair, P. Blake, A.N. Grigorenko, K.S. Novoselov, T.J. Booth, T. Stauber, N.M.R. Peres, A.K. Geim, Science **320**, 1308 (2008)
8. Y. Wang, Yi Huang, Y. Song, X. Zhang, Y. Ma, J. Liang, Y. Chen, Nano Lett. **9**, 220 (2009)
9. P. Sun, K. Wang, J. Wei, M. Zhong, Wu Dehai, H. Zhu, Nano. Res. **7**, 1507 (2014)
10. P. Chetri, B. Choudhury, A. Choudhury, J. Mater. Chem. C **2**, 9294 (2014)
11. X. Zhang, W. Zhang, X. Zhang, X. Xu, F. Meng, C.C. Tang, Adv. Cond. Matter. Phys. (2014). https://doi.org/10.1155/2014/806327
12. T. Tang, F. Liu, Y. Liu, X. Li, Xu Qinghua, Q. Feng, N. Tang, Du Youwei, Appl. Phys. Lett. **104**, 123104 (2014)
13. O.V. Kharissova, B.O. García, B.I. Kharisov, U. Méndez, Adv. Carbon Nanostruct. (2016). https://doi.org/10.5772/64319
14. H. Lee, N. Park, Y.-W. Son, S. Han, Yu Jaejun, Chem. Phys. Lett. **398**, 207 (2004)
15. S.S. Rao, S.N. Jammalamadaka, A. Stesmans, V.V. Moshchalkov, J.V. Tol, D.V. Kosynkin, A. Higginbotham-Duque, J.M. Tour, Nano Lett. **12**, 1210 (2012)
16. M.A.H. Vozmediano, M.P. López-Sancho, T. Stauber, F. Guinea, Phys. Rev. B **72**, 155121 (2005)
17. L. Pisani, B. Montanari, N.M. Harrison, New J. Phys. **10**, 033002 (2008)
18. I.S. Zhidkov, N.A. Skorikov, A.V. Korolev, A.I. Kukharenko, E.Z. Kurmaev, V.E. Fedorov, S.O. Cholakh, Carbon **91**, 298 (2015)

19. K. Pramoda, S. Suresh, H.R. Matte, A. Govindaraj, Bull. Mater. Sci. **36**, 585 (2013)
20. H. Liu, J. Huang, X. Li, J. Liu, Y. Zhang, Du Kun, Appl. Surf. Sci. **258**, 4917 (2012)
21. K.M. Daniels, A. Obe, B.K. Daas, J. Weidner, C. Williams, T.S. Sudarshan, M.V. Chandrashekhar, J. Electrochem. Soc. **163**, E130 (2016)
22. I.N. Apostolova, A.T. Apostolov, S.G. Bahoosh, J.M. Wesselinowa, J. Magn. Magn. Mater. **353**, 99 (2014)
23. N.N. Hai, P. Van Vinh, J. Phys: Conf. Ser. **187**, 012071 (2009)
24. Xiao-Hui Wei, Ralph Skomski, D. J. Sellmyer, IEEE Trans. Magn. **45**, 4089 (2009)
25. A.T. Apostolov, I.N. Apostolova, J.M. Wesselinowa, Phys. Status Solid B **255**, 1800179 (2018)
26. R. Ray, S. Biswas, S. Das, M. Patra, AIP Conf. Proc. **1447**, 319 (2012)
27. G. Hosamani, B.N. Jagadale, J. Manjanna, S.M. Shivaprasad, D.K. Shukla, J.S. Bhat, J. Mater. Sci. Mater. Electron. (2020). https://doi.org/10.1007/s10854-020-03325-7
28. M. Subramanian, P. Thakur, M. Tanemura, T. Hihara, V. Ganesan, T. Soga, K.H. Chae, R. Jayavel, T. Jimbo, J. Appl. Phys. **108**, 053904 (2010)
29. H. Coelho-Júnior, J.C. Aquino, F.H. Aragón, P. Hidalgo, R. Cohen, L.C. Nagamine, J.A. Coaquira, S.W. Da Silva, H.F. Brito, J. Nanopart. Res. **16**, 2689 (2014)
30. I.S. Roqan, S. Venkatesh, Z. Zhang, S. Hussain, I. Bantounas, J.B. Franklin, T.H. Flemban, B. Zou, J.-S. Lee, U. Schwingenschlogl, P.K. Petrov, M.P. Ryan, N.M. Alford, J. Appl. Phys. **117**, 073904 (2015)
31. S. Venkatesh, J.B. Franklin, M.P. Ryan, J.S. Lee, H. Ohldag, M.A. McLachlan, N.M. Alford, I.S. Roqan, Defect-band mediated ferromagnetism in Gd-doped ZnO thin films. J. Appl. Phys. **117**, 013913 (2015)
32. J. Bahadur, K. Pal, Phys. Low Dimens. Syst. Nanostruct. (2017). https://doi.org/10.1016/j.physe.2017.02.022
33. D.C. Marcano, D.V. Kosynkin, J.M. Berlin, A. Sinitskii, Z. Sun, A. Slesarev, L.B. Alemany, Lu Wei, J.M. Tour, ACS Nano **4**, 4806 (2010)
34. N. Nithyaa, N.V. Jaya, J. Supercond. Nov. Magn. **31**, 4110 (2018)
35. N.R. Khalid, Z. Hong, E. Ahmed, Y. Zhang, H. Chan, M. Ahmad, Appl. Surf. Sci. **258**, 5827 (2012)
36. S. Bai, S. Chen, X. Shen, G. Zhua, G. Wang, RSC Adv. **2**, 10977 (2012)
37. Pu Xipeng, D. Zhang, Y. Gao, X. Shao, G. Ding, S. Li, S. Zhao, J. Alloys Compd. **551**, 382 (2013)
38. Y. Gao, Pu Xipeng, D. Zhang, G. Ding, X. Shao, J. Ma, Carbon **50**, 4093 (2012)
39. S. Stankovich, D.A. Dikin, R.D. Piner, K.A. Kohlhaas, A. Kleinhammes, Y. Jia, Wu Yue, S.T. Nguyen, R.S. Ruoff, Carbon **45**, 1558 (2007)
40. A. Ganguly, S. Sharma, P. Papakonstantinou, J. Hamilton, J. Phys. Chem. C **115**, 17009 (2011)
41. G.K. Yogesh, E.P. Shuaib, P. Roopmani, M.B. Gumpu, U.M. Krishnan, D. Sastikumar, Diam. Relat. Mater. (2018). https://doi.org/10.1016/j.diamond.2020.107733
42. W. Chen, L. Yan, P.R. Bangal, J. Phys. Chem. C **114**, 19885 (2010)
43. R.M. Mohamed, I.A. Mkhalida, J. Alloys Compd. **501**, 143 (2010)
44. J.B. Wu, M.L. Lin, X. Cong, H.N. Liu, P.H. Tan, Chem. Soc. Rev. **47**, 1822–1873 (2018)
45. D. Wang, X. Li, J. Chen, X. Tao, Chem. Eng. J **198**, 547 (2012)
46. T. Enoki, K. Takai, Dalton Trans. (2008). https://doi.org/10.1039/b800138n
47. L.M. Pastrana-Martínez, S. Morales-Torres, V. Likodimos, J.L. Figueiredo, J.L. Faria, P. Falaras, A.M. Silva, Appl. Catal. B **123**, 241 (2012)
48. T. Kavitha, A.I. Gopalan, K.P. Lee, S.Y. Park, Carbon **50**, 2994 (2012)
49. A. Manikandan, J.J. Vijaya, M. Sundararajan, C. Meganathan, L.J. Kennedy, M. Bououdina, Superlattices Microst. **64**, 118 (2013)
50. J. Li, S.L. Zhou, G.B. Hong, C.T. Chang, Chem. Eng. J. **219**, 486 (2013)
51. A. Tayel, A.R. Ramadan, O.A. El Seoud, Catalysts **491**, 1 (2018)
52. X. Chen, S.S. Mao, Chem. Rev. **107**, 2891 (2007)
53. R.A. Rakkesh, D. Durgalakshmi, S. Balakumar, J. Mater. Chem. C **2**, 6827 (2014)
54. L. Shahriary, A.A. Athawale, International Journal of Renewable Energy and Environmental. Engineering **2**, 58 (2014)
55. Y. Alivov, T. Grant, C. Capan, W. Iwamoto, P.G. Pagliuso, S. Molloi, Nanotechnology **24**, 275704 (2013)
56. D.M. Murphy, Metal Oxide Catal. (2008). https://doi.org/10.1002/9783527626113.ch1
57. K. Thiyagarajan, K. Sivakumar, J. Mater. Sci. **52**, 8084 (2017)
58. W. Guo, B. Zhao, Q. Zhou, Y. He, Z. Wang, N. Radacsi, ACS Omega **4**, 10252 (2019)
59. C.N. Rao, H.R. Matte, K.S. Subrahmanyam, U. Maitra, Chem. Sci. **3**, 45 (2012)
60. K.P. Siqueira, P.P. Lima, R.A. Ferreira, L.D. Carlos, E.M. Bittar, F.M. Matinaga, R. Paniago, K. Krambrock, R.L. Moreira, A. Dias, J. Phys. Chem. C **119**, 17825 (2015)
61. J. Kliavaa, I. Edelmanb, A. Potseluykob, E. Petrakovskajab, R. Bergera, I. Bruckentalc, Y. Yeshurunc, A. Malakhovskiid, T. Zarubina, J. Magn. Magn. Mater. **272**, e1647 (2004)
62. S. Simon, I. Ardelean, S. Filip, I. Bratu, I. Cosma, Solid State Commun. **116**, 83 (2000)
63. Li Yang, M.L. Cohen, S.G. Louie, Phys. Rev. Lett. **101**, 186401 (2008)
64. G. Li, A. Luican, J.L. Dos Santos, A.C. Neto, A. Reina, J. Kong, E.Y. Andrei, Nat. Phys. Lett. (2009). https://doi.org/10.1038/NPHYS1463
65. W. Wei, Qu Xiaogang, Small **8**, 2138 (2012)
66. B. Das, B. Choudhury, A. Gomathi, A.K. Manna, S.K. Pati, C.N. Rao, Chem. Phys. Chem. **12**, 937 (2011)
67. N. Aggarwal, K. Kaur, A. Vasishth, N.K. Verma, J. Mater. Sci: Mater. Electron. **27**, 13006 (2016)
68. O. Oprea, O.R. Vasile, G. Voicu, L. Craciun, E. Andronescu, Dig. J. Nanomater. Biostruct. **7**, 1757 (2012)
69. K. Thiyagarajan, M. Muralidharan, K. Sivakumar, J. Supercond. Nov. Magn. **31**, 117 (2018)
70. Z. Xiang, J. Qian, Y. Zhou, F. Liu, C. Qi, X. Shi, G. Wang, S. Ye, Mater. Lett. **161**, 286 (2015)
71. E.E. Ateia, A.T. Mohamed, K. Elsayed, J. Magn. Magn. Mater. **452**, 169 (2018)
72. S. Khashan, S. Dagher, N. Tit, A. Alazzam, I. Obaidat, Surf. Coat. Tech **322**, 92 (2017)
73. S. Dutta, S.K. Pati, J. Mater. Chem. **20**, 8207 (2010)